

## GEOCHEMISTRY

# Distinctive volcanic ash–rich lacustrine shale deposition related to chemical weathering intensity during the Late Triassic: Evidence from lithium contents and isotopes

Quanyou Liu<sup>1,2\*</sup>, Peng Li<sup>2,3</sup>, Lei Jiang<sup>4</sup>, Zhijun Jin<sup>1,2</sup>, Xinpeng Liang<sup>1,2</sup>, Dongya Zhu<sup>2,3</sup>, Qian Pang<sup>2</sup>, Rui Zhang<sup>1,2</sup>, Jiayi Liu<sup>2,3</sup>

The Late Triassic Carnian Pluvial Episode (CPE) witnessed enormous climate change closely associated with volcanic activity. However, the coupling relationship between volcanic activity and climate change, which may be linked to chemical weathering, has not yet been fully uncovered. We used lithium contents and isotopes of volcanic ash (VA)-bearing lacustrine shale to constrain their deposition pathways and response to climate changes, i.e., weathering intensity, during the Late Triassic era. Elevated  $\delta^7\text{Li}$  (i.e.,  $>2.5\text{‰}$ ) and low Li contents (i.e.,  $<65 \mu\text{g/g}$ ) in shale likely document the direct depositing of volcanic lithium from airborne VA, which mainly inherited Earth's interior  $\delta^7\text{Li}$  signal. By contrast, shale yields markedly high lithium contents (i.e.,  $>135 \mu\text{g/g}$ ), alongside relatively low  $\delta^7\text{Li}$  (i.e.,  $<0\text{‰}$ ), likely implying waterborne VA dominated by intensified weathering under a super humidity climate. Hence, this study provides evidence for the differential VA-rich shale deposition model related to chemical weathering states synchronous with climate changes during the CPE period.

Copyright © 2024 The Authors, some rights reserved; exclusive licensee American Association for the Advancement of Science. No claim to original U.S. Government Works. Distributed under a Creative Commons Attribution NonCommercial License 4.0 (CC BY-NC).

## INTRODUCTION

Global climate changes, intrinsically related to large igneous provinces (LIPs), profoundly affect the biological evolutions during Earth's history, such as the end-Permian and end-Triassic mass extinctions (1, 2). Those volcanic activities would result in rapid changes in Earth's surface climate and environment (2–4), commonly associated with the widespread deposition of organic-rich black shale (4–6). However, the pathways for the deposition of volcanic materials into a water body, i.e., airborne or waterborne, have not been well understood yet, which could be closely tied to climates.

The Late Triassic Carnian Pluvial Episode [CPE; dated 234 to 232 million years (Ma) ago] (7, 8), which is also inferred as the Carnian Pluvial Phase (9) and Carnian Black Shale Event (10), has witnessed massive changes in the climate and biosphere within  $\sim 2$  Ma. The Carnian Episode was characterized by a sudden increase in rainfall in the Paleo-Tethys Ocean shelf area on land under humid climates. It has greatly shaped the animals and plants on land (11) and resulted in a switch from carbonate platforms to black shale deposition in shallow marine environments (12). Now, the trigger mechanisms for CPE are still under debate (8, 13). Many scholars have linked the CPE event to the Wrangellia LIP, which resulted in the increase of atmospheric  $\text{CO}_2$  level and temperature (8, 13), alongside negative  $\delta^{13}\text{C}$  excursions in marine carbonates (4, 9, 14). However, climate warming caused by CPE would also lead to an intensification of water circulation and, thus, an increase in continental runoff (8, 14), which was yet to be testified.

Lithium (Li)—which occurs in the form of  $\text{Li}^+$  in minerals, melts, or fluids, and has two stable isotopes ( $^7\text{Li}$  and  $^6\text{Li}$ )—is the lightest metal in nature. The lithium isotopic composition ( $\delta^7\text{Li}$ ) of the upper continental crust (UCC) is  $+0.6 \pm 0.6$  per mil (‰) ( $2\sigma$ ), which is markedly lighter than the mantle  $\delta^7\text{Li}$  value ( $+4\text{‰}$ ) (15, 16). Neither redox reactions (17) nor biological effects (18, 19) could fractionate the lithium isotopes on Earth's surface. Instead, continental chemical weathering intensity would determine  $\delta^7\text{Li}$  values of weathering products. During chemical weathering, primary mineral dissolution generates no notable Li isotopic fractionations (20, 21), whereas most of the secondary minerals (detrital clays) would adsorb or incorporate  $^6\text{Li}$ , leading to notable Li isotopic fractionations during the detrital clay formations (19, 21–23). In general, high chemical weathering intensity results in more negative  $\delta^7\text{Li}$  values in riverine detrital materials or marine sediments on continental shelves (24–27).

The Ordos Basin is a large multicycle superimposed basin located at the western part of the North China Craton in east Tethys (Fig. 1, A and B). The Yanchang Formation records the response of terrestrial sedimentary systems to climate change during the Middle-Late Triassic. We studied the Upper Triassic Chang 7 Member of the Yanchang Formation from drill core Y1011 in the Ordos Basin. Cyclic volcanic ash (VA)-rich shale deposition has been related to marked changes in atmospheric and water environments during the global CPE (28). Integrating the well-constrained age model (Fig. 1C), this drill core interval provides an unprecedented opportunity to decipher the interactions between climate change and VA-rich shale sedimentation on land during the CPE. The isopach map of tuff in Chang 7 Member is generally distributed in the northwest direction, which gradually thinning from southwest to northeast (29), implying that the volcanic eruption may have originated from the southern Qinling orogenic belt.

On the basis of lithium abundance and isotopic data (table S1), we established the sedimentary pathways of VA by referring to other geochemical proxies [i.e., total organic carbon (TOC) and carbon

<sup>1</sup>Institute of Energy, Peking University, Beijing 100871, China. <sup>2</sup>State Key Laboratory of Shale Oil and Gas Enrichment Mechanisms and Effective Development, Beijing 100083, China. <sup>3</sup>Petroleum Exploration and Production Research Institute, SINOPEC, Beijing 100083, China. <sup>4</sup>Key Laboratory of Cenozoic Geology and Environment, Institute of Geology and Geophysics, Chinese Academy of Sciences, Beijing 100029, China.

\*Corresponding author. Email: liuqy@pku.edu.cn

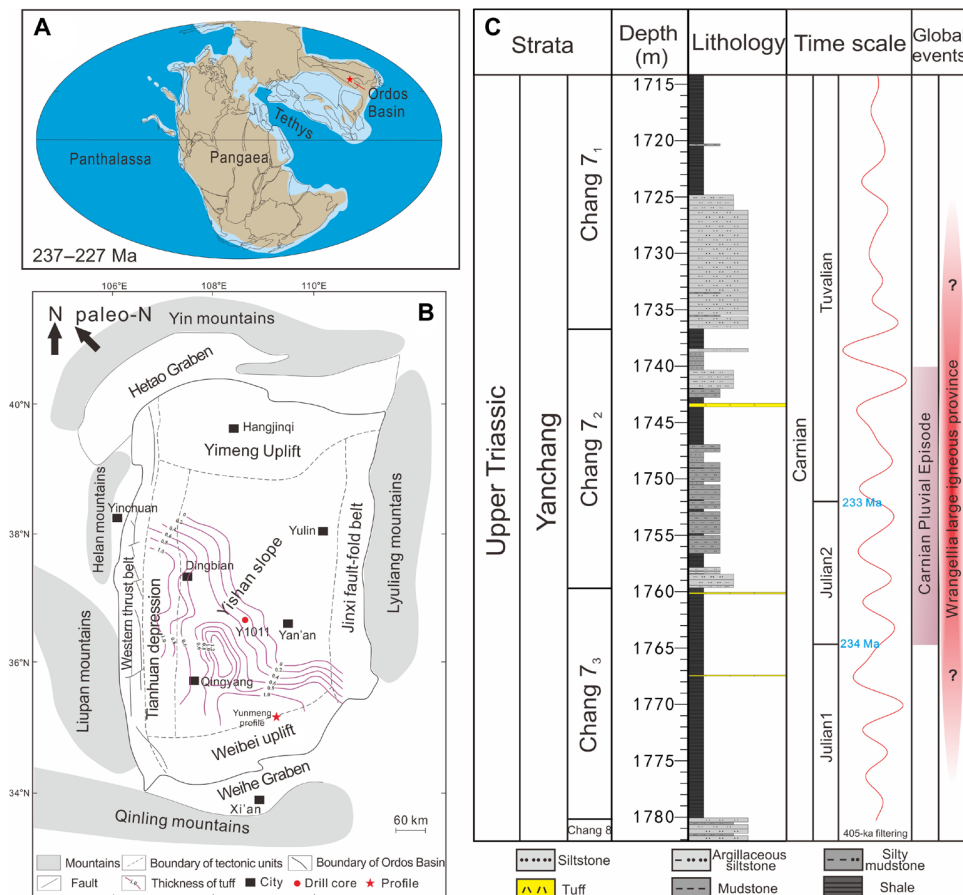


**Fig. 1. Location and geological context for the study area. (A)** Reconstructed topography in the late Middle Triassic for the Ordos Basin, modified after (31). **(B)** Location of the sampling drill core from this study, modified after (29, 71). **(C)** Stratigraphic column of the Chang 7 Member of drill core Y1011, modified after (31, 34).

isotopes] of the shale. The climate changes (i.e., weathering intensity, volcanic intensity, and sedimentation rate) during the CPE were further reconstructed. Specifically, the crucial effects of climate change on the shale deposition model were revealed, which has notable implications for its related petroliferous resources.

## RESULTS

Samples were collected from the drill core Y1011 ( $36^{\circ}37'12''N$ ,  $108^{\circ}37'48''E$ ) at the Yishan Slope of the southern Ordos Basin (Fig. 1B). The selected samples were subjected to detailed sedimentology and petrology and analyzed for major and trace element measurements ( $n = 162$ ), TOC ( $n = 164$ ), total nitrogen (TN), and organic carbon isotope ( $\delta^{13}\text{C}_{\text{org}}$ ) measurements ( $n = 161$ ), as well as Li contents ( $n = 91$ ) and Li isotopes ( $n = 83$ ).

## Time scale

The stratigraphic correlation of Chang 7 Member is established by the combination of U-Pb isotopic ages of zircon, astronomical cycles, and spore-pollen assemblages. A 405-ka-long eccentricity (30) tuned floating astrochronological time scale, anchored with a zircon U-Pb dating age of  $234.1 \pm 2.4$  Ma obtained from the tuff layer (28) of the studied interval, allows us to calculate the age of the lower boundary of the Chang 7 Member is 235.3 Ma, with a deposition

duration of about 5 Ma for the entire interval (31). On the basis of this age model, the onset time of the CPE event in this drill core interval is 234.0 Ma (Fig. 1C), broadly coinciding with the Carnian palynostratigraphic study of the drill core Y1011 and Yunmeng profile (28, 32, 33). Both the zircon U-Pb ages and the spore-pollen fossils of Chang 7 Member are comparable with those of Tanzhuang and Anyao Formations ( $232.9 \pm 2.1$  and  $233.1 \pm 1.3$ ) in Jiyuan Basin (adjacent to the Ordos Basin), which systematically recorded the CPE (34, 35).

## Sedimentology and petrology

From bottom to top, the Chang 7 Member can be divided into three sub-members (Chang 7<sub>1–3</sub>) according to periodic changes in lithology controlled by sedimentary cycles (36). The Chang 7<sub>3</sub> submember in drill core Y1011 consists mainly of a set of black organic-rich shale (depth of ~1769 to 1780 m) with some coarse-grained clastics locally associated with tuff deposition (depth of 1759.5 to 1769 m; Fig. 1 and fig. S1). Two thin tuff layers were developed in the black shale interval with fine-grained clastics of thicknesses of approximately 10 and 15 cm, respectively. The Chang 7<sub>2</sub> submember (depth of ~1737 to 1759 m) mainly consists of gray silty mudstone, with laminated black organic-rich shale occurring in the upper part (depth of 1737 to 1747 m; Fig. 1). Notably, an approximately 35-cm-thick tuff layer within shale was found in this submember.

The Chang 7<sub>1</sub> submember lies between depths of ~1715 and 1737 m, with the lower and upper parts mainly consisting of gray argillaceous siltstone (~1737 to 1725 m) and black mudstone (~1725 to 1715 m), respectively. Not any tuff deposition was observed in the Chang 7<sub>1</sub> submember.

The tuff from the Chang 7 Member mainly occurs as grayish-yellow and is supported by a miscellaneous matrix with a clear interface with the shale (fig. S1, A and B). Tuff comprises glass, crystals, and rock debris, with particle sizes commonly less than 2 mm, shapes ranging from elliptical to angular and, thus, uneven sorting. Specifically, some glass fragments display arc, sickle, and chicken bone shapes, suggesting products of volcanic fragments deposited in a water body (37, 38). Notably, some tuffs, which were dominated by clay minerals (fig. S1C), were altered into bentonite.

### Li contents and isotopes

The lithium contents (from 2.91 to 263.23  $\mu\text{g/g}$ , average at 63.04  $\mu\text{g/g}$ ) and isotopes (from  $-5.59$  to  $+12.99\text{\textperthousand}$ ) display large variations in our study interval (Fig. 2 and fig. S2). The Li isotopes of the Chang 7 shale mainly vary from a Li-rich, low- $\delta^7\text{Li}$  endmember ( $\delta^7\text{Li}$  of  $-0.5 \pm 1\text{\textperthousand}$  and Li/Al of  $1.0 \pm 0.1 \times 10^{-3}$ ) to a Li-poor, high- $\delta^7\text{Li}$  endmember ( $\delta^7\text{Li}$  of  $3.5 \pm 1.5\text{\textperthousand}$ , Li/Al of  $0.30 \pm 0.12 \times 10^{-3}$ ) (25). A decreasing trend of  $\delta^7\text{Li}$  along with decreased lithium contents is observed in samples with lithium contents below 50  $\mu\text{g/g}$ . While samples exhibit abnormally high lithium contents (i.e.,  $>135 \mu\text{g/g}$ ), they commonly yield relatively low  $\delta^7\text{Li}$  average at  $-2.25\text{\textperthousand}$ .

To exclude the impact of grain size changes on lithium isotope fractionation (24), we selected fine-grained sediments mainly composed of silty mudstone and shale, as supported by the Al/Si values that are mainly above 0.3 (fig. S3). The lithium isotopes and contents exhibit continuous changes between two endmember thresholds: igneous rock versus sediments dominated by shale (fig. S2). This may imply that the pluses enrichment of  $\delta^7\text{Li}$  was related to volcanic activity during the Chang 7 shale deposition. Therefore, the  $\delta^7\text{Li}$  values of shale in the study interval were not mainly controlled by the silicate weathering intensity as other factors, such as evaporite and volcanic activity, may be central in controlling the Li contents and  $\delta^7\text{Li}$  values in these shale (39–41).

Given the fact that the detrital Li isotope is sensitive to diagenesis and maturity, we have carried out a systematic analysis of the thermal maturity and potassium content of Chang 7 shale. The value of vitrinite reflectance (Ro) for Chang 7 shale in the study area ranges from 0.84 to 1.02% with an average of 0.91%, which is already in the mesodiagenetic stage. The perfectly positive correlation between Ro values and the burial depth is observed (fig. S4). Considering the small slope of the formation, the thermal maturity with buried depth should vary in a small range. Moreover, the thickness of the interval of drill core Y1011 in this study is no more than 50 m and is in a similar stage of thermal maturity on the whole, which cannot cause the relatively large fractionation of lithium isotopes. The K/Al ratio of Chang 7 shale ranges from 0.18 to 0.38, with an average of 0.27, showing no unusual changes. The A-CN-K chart of the studied

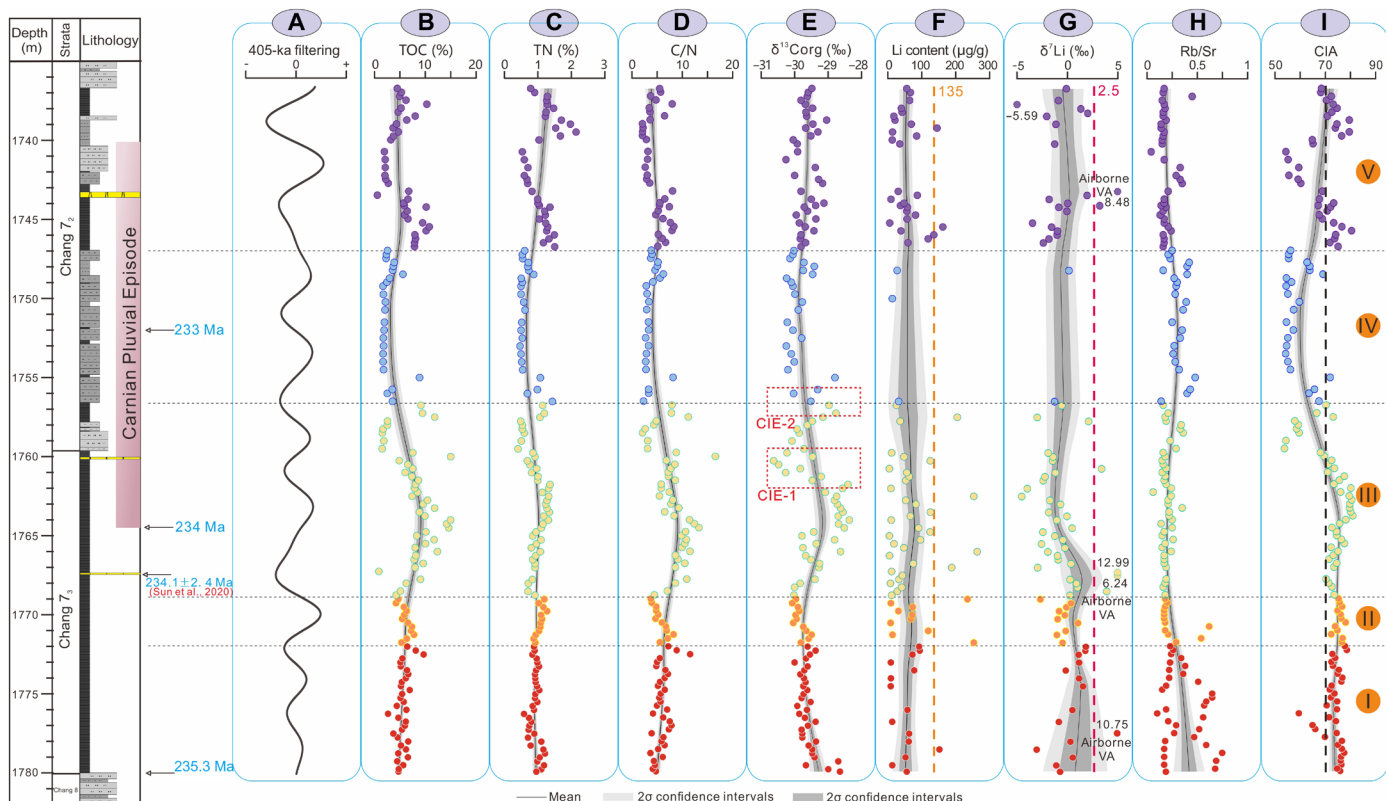


**Fig. 2. Changes in the paleoclimate and paleoenvironment under chemical weathering and volcanism based on lithium contents and isotopes.** (A) Floating astrochronological time scale of the studied core (31). The records of (B) TOC values. (C) TN values. (D) C/N ratio. (E)  $\delta^{13}\text{C}_{\text{org}}$  values. (F) Li content values. (G)  $\delta^7\text{Li}$  values. (H) Rb/Sr ratio. (I) CIA index.

samples (fig. S5) is similar to the Fedo's pattern (42), which does not show appreciable effects of K metasomatism. Furthermore, through the analysis of the relationship between the K/Al ratio and lithium isotope and lithium content, there are no obvious correlations (fig. S6). All evidence supports the notion that the K metasomatism of Chang 7 shale is negligible and has no control effect on lithium isotope fractionation.

The correlations between the lithium isotopes and contents (Fig. 3A), as well as between lithium isotopes and Al/Si ratios (Fig. 3B), of modern large river systems, volcanic eruptions, and Chang 7 sediments, implying that the relatively higher  $\delta^{7}\text{Li}$  values ( $>2.5\text{\textperthousand}$ ) of shale may have been related to VA (Fig. 3B) in a riverine deposition system (24, 25, 43–45). In contrast, shales are characterized by relatively low  $\delta^{7}\text{Li}$  values (i.e.,  $<0\text{\textperthousand}$ ) and abnormally high lithium contents (i.e.,  $>135 \mu\text{g/g}$ ) compared with the river sediments and regolith profiles (24, 25, 46), implying that VA associated with those shale is mainly waterborne and related to chemical weathering.

According to the lithium content and isotopic composition values, the study core interval is subdivided into five distinctive stages (I to V; Fig. 2). Stage I (1772 to 1780 m) is dominated by black shale and characterized by relatively stable lithium content with low lithium isotope values ( $\sim 0\text{\textperthousand}$ ). In general, stage II (1769 to 1772 m) yields comparable lithium isotopes as stage I, with abnormal lithium enrichment locally. Stage III (1756.7 to 1769 m), which is characterized by strongly fluctuated lithium contents and relatively low  $\delta^{7}\text{Li}$  (mainly below  $0\text{\textperthousand}$ ), contains thin tuff layers. Stage IV is characterized by markedly low lithium contents and lithium isotopes ( $\sim 0\text{\textperthousand}$ ), as well as lack of tuff layer deposition. Although the lithium contents and isotopes are generally low in stage V as well, it is intersected with sporadic marked high  $\delta^{7}\text{Li}$ , i.e., at depths of 1743.22 and 1744.12 m. Note that markedly elevated  $\delta^{7}\text{Li}$  are observed in the lower part of stage I and stage III, which is commonly associated with decreased Li contents and VA deposition (Fig. 2). It should also be noted that the co-occurrence of markedly elevated lithium

contents with depleted  $\delta^{7}\text{Li}$  values in stage II and stage III (i.e., depths of 1778.5, 1757.5, 1762.5, 1766, and 1767 m) coincides with the presence of cryptotephra (invisible VA layers).

### TOC, C/N, and $\delta^{13}\text{C}_{\text{org}}$

The TOC (0.20 to 14.87%, average at 5.22%) and TN (0.20 to 2.12%, average at 0.89%) also exhibit strong heterogeneity but general synergistic changes in this drill core interval (Fig. 2). Both TOC and TN are relatively stable in stages I and II while fluctuates strongly in stage III before decreasing to the lowest values in stage IV. This trend is likely related to lithology changing from shale to mudstone and then to sandstone-dominated sediments. The TOC and TN values in stage V yield large variations that are closely related to lithology changes as well.

The  $\delta^{13}\text{C}_{\text{org}}$  values range from  $-30.6$  to  $-26.5\text{\textperthousand}$ , with an average of  $-29.5\text{\textperthousand}$ , in this interval. The  $\delta^{13}\text{C}_{\text{org}}$  values in stages I and II are relatively stable, with an average value of  $-29.7\text{\textperthousand}$ . By contrast, stage III displays fluctuating  $\delta^{13}\text{C}_{\text{org}}$  values with two large carbon isotope excursions (CIE-1 and CIE-2) from  $-28.4$  to  $-30.63\text{\textperthousand}$  and from  $-28.76$  to  $-30.03\text{\textperthousand}$ , respectively. The  $\delta^{13}\text{C}_{\text{org}}$  values and trends observed in stages IV and V are similar to those observed in stages I and II.

## DISCUSSION

### Interpretation of TOC, TN, C/N, and $\delta^{13}\text{C}_{\text{org}}$ data

The general high nitrogen content in the shale-dominated interval of the Chang 7 Member suggests a relatively high paleoproductivity (47). Shale deposition was superposed with several active volcanic events, as indicated by abundant VA layers (mainly tuff and its alteration product, bentonite), associated with abnormally high lithium isotope values (fig. S1) (48). In addition, the stratigraphic covariations of the TOC, TN, and C/N ratio likely indicate the mutual transformation of organic matter from terrestrial plants to aquatic organisms during shale deposition (49, 50). The C/N ratios

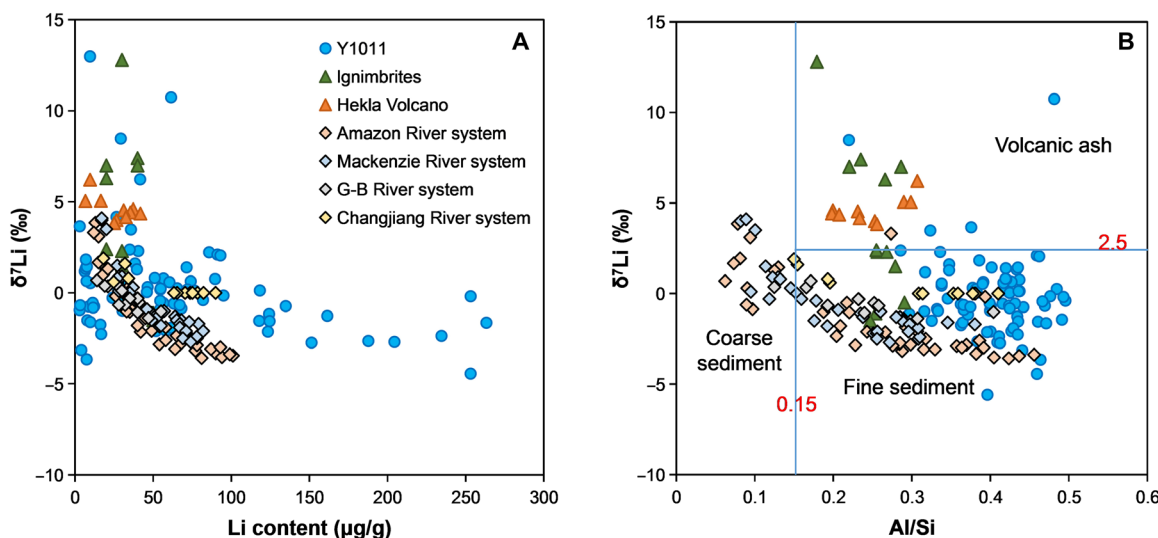


**Fig. 3. The compilation of Li isotopic composition vs. Li content and Al/Si ratio in river sediments, volcanic ash, and Chang 7 sediments.** (A) Li isotopic composition versus Li content: VA has relatively high  $\delta^{7}\text{Li}$  values and low lithium contents compared with the river sediments, modified after (24, 43–45). (B) Li isotopic composition versus Al/Si ratio: When an Al/Si ratio of 0.15 is used to distinguish coarse-grained and fine-grained sediments, VA can be identified with elevated  $\delta^{7}\text{Li}$  ( $>2.5\text{\textperthousand}$ ), modified after (24).

range from 1.20 to 16.67, with an average of 5.73, suggesting that aquatic organisms may have played a dominant role in shale deposition (51). Some elevated C/N ratios (i.e., an average of 9.21 at depths from 1760 to 1768 m in stage III) may indicate the highly degraded aqueous algal materials (52).

Two negative carbon excursions (CIE-1 and CIE-2) are observed during the CPE event in the study interval. The CIE-1 was likely related to massive volcanic CO<sub>2</sub> emissions and consequent climatic warming (14, 53). Massive isotopically light CO<sub>2</sub> entering the atmosphere will cause a strong greenhouse effect and global warming, which generates global negative CIEs widely recorded in both the lacustrine (34) and marine sediment profiles (7, 8, 14). In contrast, the subsequent CIE-2 was most plausibly due to the varying contributions from terrestrial and algal organic carbon, as revealed by the covariations of the C/N ratios and  $\delta^{13}\text{C}_{\text{org}}$  (fig. S7).

### Li contents and isotopes controlled by chemical weathering intensity

Rb/Sr ratio of riverine sediments is an effective proxy for identifying the paleoclimate states (54). Under humid climates, increased precipitation and weathering intensity would lead to the accumulation of large amounts of Sr, resulting in a decreased Rb/Sr ratio in the lake sediments (55). By contrast, under relatively dry climate conditions, lake sediments would display high Rb/Sr ratios predominantly due to the low precipitation with decreased weathering intensity (56). In the study interval, neither the lithium contents nor the lithium isotopes coincided with the varying Rb/Sr ratios, indicating that lithium enrichment and lithium isotope fractionation (Fig. 4, A and B) may not simply be related to climate states, i.e., arid and humid climates (55, 56). However, both lithium contents and isotopes are positively correlated with the Rb/Sr ratio [fig. S8; coefficient of

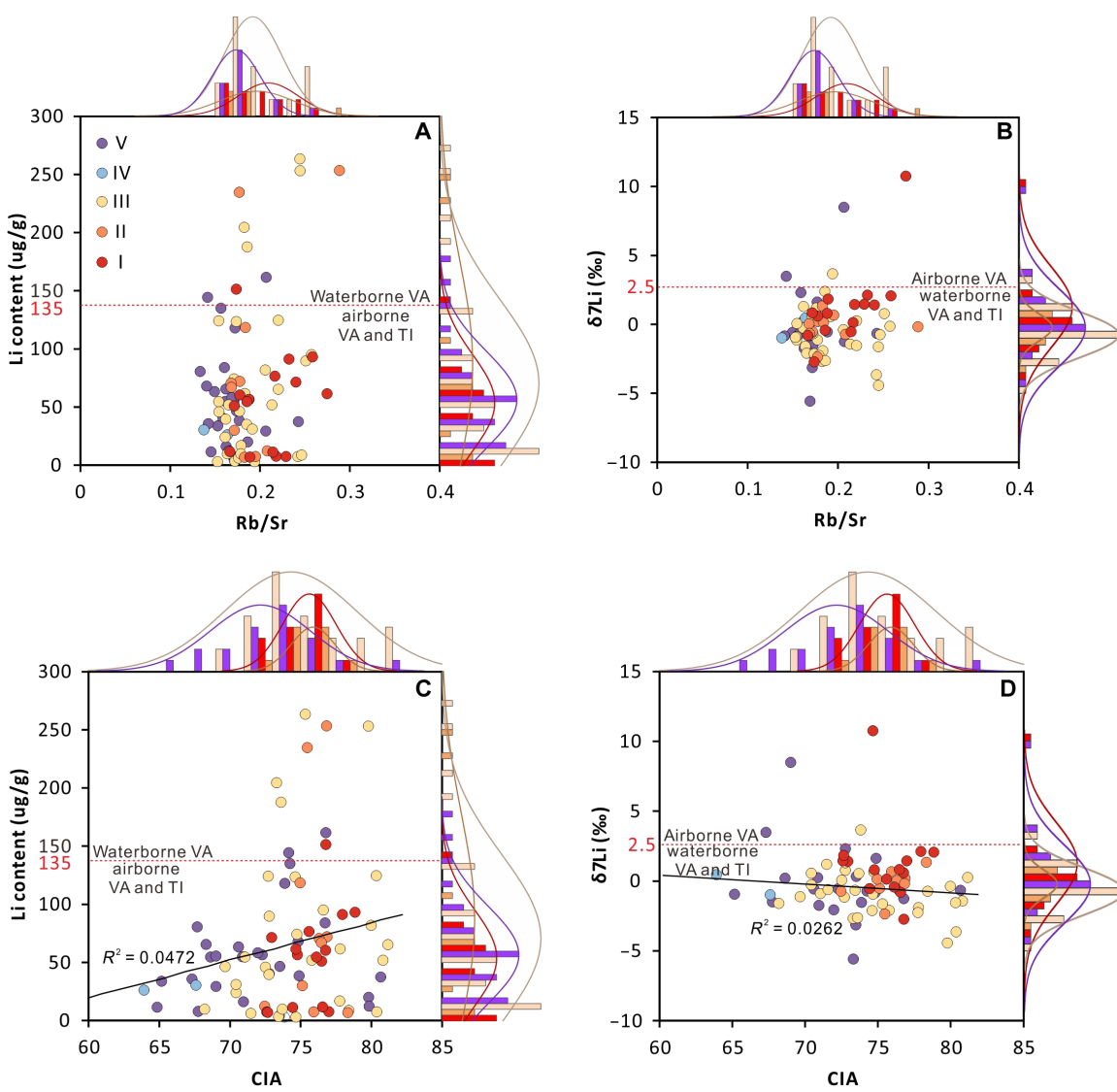


**Fig. 4. Correlation of lithium content and isotope with Rb/Sr and CIA for Late Triassic Chang 7 lacustrine shale in drill core Y1011, Ordos Basin.** (A) Rb/Sr ratio versus lithium content: No notable correlation was observed, but there were slight differences between stages. (B) Rb/Sr ratio versus  $\delta^{7}\text{Li}$ : No obvious correlation was observed, and the effect of climate on lithium isotope fractionation was not obvious. (C) CIA versus lithium content: No obvious correlation was observed ( $R^2 = 0.0472$ ). (D) CIA versus  $\delta^{7}\text{Li}$ : No obvious correlation was observed ( $R^2 = 0.0262$ ).

determination ( $R^2$ ) are 0.5882 and 0.1604] in waterborne VA-rich shale with lithium contents greater than 135 µg/g. Together with their relatively low  $\delta^7\text{Li}$  values (average at  $-2.25\text{\textperthousand}$ ), being close to the average  $\delta^7\text{Li}$  values of the UCC [ $+0.6 \pm 0.6\text{\textperthousand}$  ( $2\sigma$ )] (15), suggest that those high Li contents and low  $\delta^7\text{Li}$  values were most plausibly related to enhanced weathering of VA-rich sediments.

The chemical index of alteration (CIA) is another effective proxy to reflect the degree of chemical weathering of in situ materials (i.e., paleosols) and transported sediments (57). The equation for the CIA is listed as

$$\text{CIA} = [\text{Al}_2\text{O}_3 / (\text{Al}_2\text{O}_3 + \text{CaO}^* + \text{Na}_2\text{O} + \text{K}_2\text{O})] \times 100$$

where all oxides are in molar units, and  $\text{CaO}^*$  represents only CaO in the silicate fraction and no CaO is present in apatite and carbonate (42).

The poor correlations between CIA and Li contents ( $R^2 = 0.0472$ ), as well as between CIA and  $\delta^7\text{Li}$  values ( $R^2 = 0.0262$ ; Fig. 4, C and D), further confirm that the impact of chemical weathering on lithium enrichment and lithium isotope fractionation may be insignificant. A relatively good relationship between Li contents and CIA is observed in samples with low Li contents (<50 µg/g; fig. S9;  $R^2$  is 0.1017), which correlated well with the  $\delta^7\text{Li}$  values (fig. S2), indicating the weathering of regolith near igneous rock (25, 46). Hence, the VA-bearing shales with low Li contents are likely related to lacustrine shale deposition under relatively dry climates, which is characterized by low weathering intensity with high airborne VA input.

The cyclic VA-rich shales with abundant tuff deposition in the study interval are likely sourced from the Triassic volcanic rocks in the Qinling orogenic belt (fig. S5) (48). Some tuff-bearing layers, along with markedly elevated CIA values, imply that they are likely related to enhanced chemical weathering (42, 57–59). By contrast, the airborne VA, which entered the waterbody directly from the atmosphere, displaying low lithium contents and isotopes in their associated shale. Large fluctuations of the Rb/Sr ratio (from 0.10 to 0.75; Fig. 2) in stage I may be related to the rapid changes between humid and arid climates (60), with these climatic droughts further exacerbated by volcanic activity (61). A sharp decrease in CIA after the volcanic activity appears to indicate the coupling of climate change and chemical weathering intensity. The Rb/Sr ratios in stage II maintained at low levels (generally less than 0.2), implying that the climate may have changed from monsoon (humid-drought) to humid, as revealed by relatively high CIA values (>70; Fig. 2), a manifestation of increased chemical weathering intensity. The average Rb/Sr ratio of 0.31, along with low CIA values, implies a relatively arid climate with low chemical weathering intensity during stage IV deposition, followed by a humid climate and then a dry climate period interrupted by volcanic activity during stage V deposition (Fig. 2). Notably, a large shift of lithium isotopes (approaching 20‰) in the study interval could be best explained by different sediment sources and processes (i.e., large lithium isotope fractionation) related to chemical weathering intensity due to climate changes during shale deposition (19, 25, 62).

### Distinctive shale deposition models related to climate change

We further propose two differential shale deposition and lithium cycling models associated with tuff deposition that were closely related to volcanic activity and climate changes during the Late

Triassic era (Fig. 5). In our case, VA was most likely sourced from the Qinling orogenic belt rather than from the Wrangellia LIP (4), according to the evolution of the Neo-Tethys plate (63). During stage I deposition, the weathering intensity was relatively weak, as indicated by the relatively stable  $\delta^{13}\text{C}_{\text{org}}$  and lithium contents, with  $\delta^7\text{Li}$  values below 2.5‰ (Fig. 5A), implying a cold and dry climate (64). The shales deposited in the lake were mainly sourced from aquatic organisms under relatively high paleoproductivity conditions (49) with elevated nutrient inputs from volcanic materials (5). By contrast, markedly elevated lithium contents in stage II, i.e., 253.17 µg/g at 1771.75 m and 234.50 µg/g at 1769 m, could most plausibly be explained by the notably increased terrigenous inputs related to the intralanding flood events under a heavy rainfall climate (Fig. 5B). As Zhu *et al.* (65) state, the high-temperature, high-rainfall climate allows the rapid input of terrestrial materials and thus the phosphorus into the lakes and oceans, boosting primary

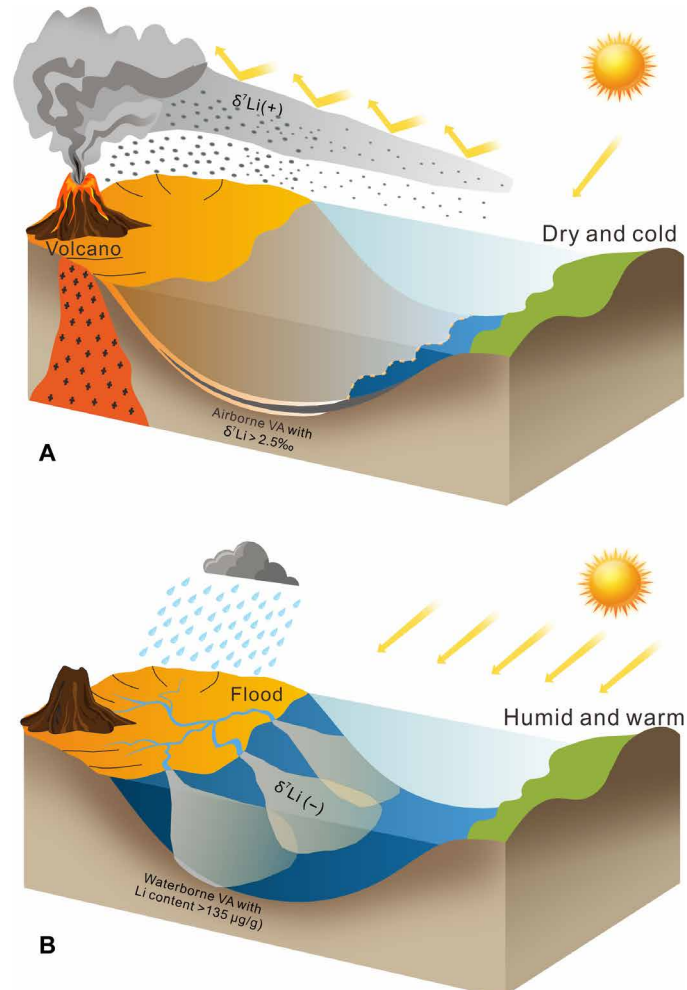


**Fig. 5. Model for shale deposition and lithium cycling of the Chang 7 Member from the Ordos Basin.** (A) Volcanic eruption brought the deep  ${}^7\text{Li}$ -rich volatility into the atmosphere, obscured the sunlight, and led to a cold and dry climate, along with airborne VA deposition characterized by elevated  $\delta^7\text{Li}$  ( $>2.5\text{\textperthousand}$ ). (B) Heavy rainfall-induced floods led to an enhanced chemical weathering intensity, resulting in markedly increased waterborne lithium content ( $>135\text{ }\mu\text{g/g}$ ) by leaching of terrigenous volcanic-bearing matters.

productivity and organic carbon burial. Those elevated lithium content shale intervals are commonly associated with high TN values, implying a relatively high paleoproductivity. While a synergistic decrease of the C/N ratio and TOC values in this interval thus implies a decreased terrigenous input. Nevertheless, shale deposition was primarily sourced from terrigenous organic matter during this period.

Notably, the observation of some elevated  $\delta^7\text{Li}$  (i.e., >2.5‰) before the onset of the CPE in stage III suggests the existence of a short period of cold and dry climate before this major event. However, when entering into the CPE, the shale samples display markedly high lithium contents (>135 µg/g) along with relatively low  $\delta^7\text{Li}$ , suggesting the dominance of a warm and humid climate with an increased chemical weathering intensity. Several positive carbon isotope excursions and the notably increased TOC (up to 14.87%) and TN (exceeding 1%) values suggest a markedly elevated terrigenous organic matter input (49) under such a long-term humid climate. The set of coarse-grained argillaceous siltstones deposited in stage IV could also be related to the delta deposition under heavy rainfall conditions. This humid climate may have extended into stage V deposition, which is interrupted by short periods of cold and dry climate as indicated by the local presence of airborne VA with elevated  $\delta^7\text{Li}$  values (Fig. 2).

Hence, this study emphasizes that the Li content and  $\delta^7\text{Li}$  of Triassic lacustrine shale are effective toolkits to uncover their deposition models, which are closely linked to strongly fluctuated climates during the CPE event likely related to active volcanic events. Specifically, the elevated  $\delta^7\text{Li}$  (>2.5‰) with low Li content (i.e., <65 µg/g) and markedly high Li content (>135 µg/g) with low  $\delta^7\text{Li}$  (i.e., <0‰) in shale represents an arid climate associated with airborne VA and a heavy rainfall climate associated with waterborne VA, respectively. Notably, these climate-related geological events would have markedly enhanced the paleoproductivity of the lake, boosted shale deposition dominated either by terrestrial or aquatic organic matters. Hence, our findings have practical significance for lacustrine shale oil and gas exploration and are able to provide useful guidelines for the prediction and exploitation of those energy resources (48, 66, 67).

## MATERIALS AND METHODS

One hundred sixty-eight core samples were collected from drill core Y1011 in the southern Ordos Basin. The samples selected for this study were shale, mudstone, sandstone, and tuff.

### Thin section observation

Thin sections of the Chang 7 tuff and shale samples were analyzed at the State Key Laboratory of Shale Oil and Gas Enrichment Mechanisms and Effective Development (SINOPEC) by optical microscopy using a LEICA DM4500P optical microscope.

### Organic $\delta^{13}\text{C}$ analysis

Approximately 5 to 50 g of homogeneous rock powder were decarbonated with 10% HCl at room temperature for 24 hours under episodic agitation (68). The pH of the supernatant was measured before washing with HCl. When the pH was close to 7, additional acid was added to ensure complete carbonate dissolution. After the carbonate was completely dissolved, insoluble residues were washed with deionized water until neutral and dried in an oven at 60°C. The

organic carbon isotope compositions ( $\delta^{13}\text{C}_{\text{org}}$ ) were determined online using an elemental analyzer (Flash EA2000) coupled with a Thermo Fisher MAT 253 IRMS at the State Key Laboratory GPMR at China University of Geosciences (Wuhan). The temperature of the flash combustion was set at 1050°C, whereas the reduction furnace was fixed at 680°C. Standards GBW04407 ( $\delta^{13}\text{C}_{\text{org}} = -22.4\text{\textperthousand}$ ) and GBW04408 ( $\delta^{13}\text{C}_{\text{org}} = -36.9\text{\textperthousand}$ ) were used to calibrate the carbon isotope analyses. The analytical accuracy was better than  $\pm 0.1\text{\textperthousand}$  ( $1\sigma$ ) based on multiple standards and duplicate sample analyses.

### Major and trace elements

Major and trace elements in the SKL-GPMR were analyzed using PANalytical Zetium X-ray fluorescence and an Agilent 7500a inductively coupled plasma mass spectrometer (ICP-MS), respectively, following the method of Zhang *et al.* (69). The major elements were measured using the wavelength dispersion method after fusing the powdered samples into glass beads. Trace elements were measured after acid digestion of the sample powder using  $\text{HNO}_3$  and hydrofluoric acid (HF). The average analytical uncertainty of major elements was better than 5% [relative standard deviation (RSD)] based on repeated analyses of national standards GBW07132, GBW07133, and GBW07407 and was better than 2% (RSD) for trace elements based on analyses of international standards AGV-2, BHVO-2, BCR-2, and GSR-1.

### TOC and TN

TOC and TN were measured using an Elementar Vario EL cube EA with decarbonated samples following the method of Chen *et al.* (47). Quality control checks were performed on every 10th sample, including sample duplicates, analysis of certified reference materials (acetanilide), and analysis of blanks. The measurement precision was better than  $\pm 0.1$  wt % for TOC and  $\pm 0.3$  wt % for TN.

### Li content and isotope analysis

The Li isotope analysis was performed at the Yale University following the method described by Kalderon-Asael *et al.* (70). Sample splits were evaporated to dryness and then dissolved in 1 ml of 0.2 N HCl before being loaded directly onto 2.7 ml of Bio-Rad AG50W-X12 (200 to 400 mesh) cation exchange resin, precleaned with 6 N HCl and 2× MQ  $\text{H}_2\text{O}$ , and preconditioned with 0.2 N HCl. Matrix elements were eluted with 0.2 N HCl, and then Li was released from the cation exchange resin by 0.2 N HCl. After evaporating the sample to dryness again, 5%  $\text{HNO}_3$  was added to the samples by first adding distilled  $\text{HNO}_3$  (left sealed on a hotplate at 60°C for 30 min) and then diluting the solution with 2× MQ  $\text{H}_2\text{O}$  to the desired content. A split of 100 µl was taken, and 900 µl of 2× MQ  $\text{H}_2\text{O}$  was added. These solutions were used to determine the Li content following column chromatography. The Li post-column contents and isotopic compositions were measured using a Thermo Finnigan Neptune Plus ICP-MS instrument at the Yale University. Li isotope data were collected at a low resolution in one block, 50 cycles per block, and 5-s integration per cycle. A standard-sample-standard bracketing technique was used to correct for mass bias and instrument fractionation using the L-SVEC-1 standard, and the sample values were calculated on the basis of the bracketing standard values. Standards were processed for each sample set to monitor the long-term reproducibility of the procedure. A typical SE of a single measurement was 0.11‰ ( $1\sigma$ ).

**Supplementary Materials****This PDF file includes:**

Supplementary Text  
Figs. S1 to S9  
Legend for table S1  
References

**Other Supplementary Material for this manuscript includes the following:**

Table S1

**REFERENCES AND NOTES**

- V. E. Courtillot, P. R. Renne, On the ages of flood basalt events. *C. R. Geosci.* **335**, 113–140 (2003).
- P. B. Wignall, Large igneous provinces and mass extinctions. *Earth-Science Reviews* **53**, 1–33 (2001).
- Z. Guo, J. Liu, S. Sui, Q. Liu, H. He, Y. Ni, The mass estimation of volatile emission during 1199–1200 AD eruption of Baitoushan volcano and its significance. *Science in China Series D: Earth Sciences* **45**, 530 (2002).
- J. Dal Corso, P. Mietto, R. J. Newton, R. D. Pancost, N. Preto, G. Roghi, P. B. Wignall, Discovery of a major negative  $\delta^{13}\text{C}$  spike in the Carnian (Late Triassic) linked to the eruption of Wrangellia flood basalts. *Geology* **40**, 79–82 (2012).
- S. Duggen, P. Croot, U. Schacht, L. Hoffmann, Subduction zone volcanic ash can fertilize the surface ocean and stimulate phytoplankton growth: Evidence from biogeochemical experiments and satellite data. *Geophys. Res. Lett.* **34**, (2007).
- B. Langmann, K. Zakšek, M. Hort, S. Duggen, Volcanic ash as fertiliser for the surface ocean. *Atmos. Chem. Phys.* **10**, 3891–3899 (2010).
- J. Dal Corso, N. Preto, C. Agnini, S. Hohn, A. Merico, H. Willemse, P. Gianolla, Rise of calcispheres during the Carnian Pluvial Episode (Late Triassic). *Global Planet. Change* **200**, 103453 (2021).
- Y. D. Sun, P. B. Wignall, M. M. Joachimski, D. P. G. Bond, S. E. Grasby, X. L. Lai, L. N. Wang, Z. T. Zhang, S. Sun, Climate warming, euxinia and carbon isotope perturbations during the Carnian (Triassic) Crisis in South China. *Earth Planet. Sci. Lett.* **444**, 88–100 (2016).
- S. Mueller, M. Hounslow, W. Kürschner, Integrated stratigraphy and palaeoclimate history of the Carnian Pluvial Event in the Boreal realm; new data from the Upper Triassic Kapp Toscana Group in central Spitsbergen (Norway). *J. Geol. Soc. London* **173**, 186–202 (2016).
- T. Hornung, R. Brandner, Biochronostigraphy of the Reingraben Turnover (Hallstatt Facies Belt): Local black shale events controlled by regional tectonics, climatic change and plate tectonics. *Facies* **51**, 460–479 (2005).
- M. Simms, A. Ruffell, Synchronicity of climatic change and extinctions in the Late Triassic. *Geology* **17**, 265 (1989).
- J. G. Ogg, Z. Q. Chen, M. J. Orchard, H. S. Jiang, in *Geologic Time Scale 2020*, F. M. Gradstein, J. G. Ogg, M. D. Schmitz, G. M. Ogg, Eds. (Elsevier, 2020), pp. 903–953.
- J. Trotter, I. Williams, A. Nicora, M. Mazza, M. Rigo, Long-term cycles of Triassic climate change: A new  $\delta^{18}\text{O}$  record from conodont apatite. *Earth Planet. Sci. Lett.* **415**, 165–174 (2015).
- J. Dal Corso, P. Gianolla, R. J. Newton, M. Franceschi, G. Roghi, M. Caggiati, B. Rauczik, T. Budai, J. Haas, N. Preto, Carbon isotope records reveal synchronicity between carbon cycle perturbation and the “Carnian Pluvial Event” in the Tethys realm (Late Triassic). *Global Planet. Change* **127**, 79–90 (2015).
- L. Sauzéat, R. L. Rudnick, C. Chauvel, M. Garçon, M. Tang, New perspectives on the Li isotopic composition of the upper continental crust and its weathering signature. *Earth Planet. Sci. Lett.* **428**, 181–192 (2015).
- F.-Z. Teng, R. L. Rudnick, W. F. McDonough, S. Gao, P. B. Tomascak, Y. Liu, Lithium isotopic composition and concentration of the deep continental crust. *Chem. Geol.* **255**, 47–59 (2008).
- F. Faure, P. Schiano, Experimental investigation of equilibration conditions during forsterite growth and melt inclusion formation. *Earth Planet. Sci. Lett.* **236**, 882–898 (2005).
- E. Lemarchand, F. Chabaux, N. Vigier, R. Millot, M.-C. Pierret, Lithium isotope systematics in a forested granitic catchment (Strengbach, Vosges Mountains, France). *Geochim. Cosmochim. Acta* **74**, 4612–4628 (2010).
- R. L. Rudnick, P. B. Tomascak, H. B. Njo, L. R. Gardner, Extreme lithium isotopic fractionation during continental weathering revealed in saprolites from South Carolina. *Chem. Geol.* **212**, 45–57 (2004).
- A. Verney-Carron, N. Vigier, R. Millot, Experimental determination of the role of diffusion on Li isotope fractionation during basaltic glass weathering. *Geochim. Cosmochim. Acta* **75**, 3452–3468 (2011).
- J. Wimpenny, C. A. Colla, P. Yu, Q.-Z. Yin, J. R. Rustad, W. H. Casey, Lithium isotope fractionation during uptake by gibbsite. *Geochim. Cosmochim. Acta* **168**, 133–150 (2015).
- J. Wimpenny, S. R. Gíslason, R. H. James, A. Gannoun, P. A. E. Pogge Von Strandmann, K. W. Burton, The behaviour of Li and Mg isotopes during primary phase dissolution and secondary mineral formation in basalt. *Geochim. Cosmochim. Acta* **74**, 5259–5279 (2010).
- R. S. Hindshaw, R. Tosca, T. L. Goût, I. Farnan, N. J. Tosca, E. T. Tipper, Experimental constraints on Li isotope fractionation during clay formation. *Geochim. Cosmochim. Acta* **250**, 219–237 (2019).
- M. Dellinger, J. Gaillardet, J. Bouchez, D. Calmels, V. Galy, R. G. Hilton, P. Louvat, C. France-Lanord, Lithium isotopes in large rivers reveal the cannibalistic nature of modern continental weathering and erosion. *Earth Planet. Sci. Lett.* **401**, 359–372 (2014).
- M. Dellinger, J. Bouchez, J. Gaillardet, L. Faure, J. Moureau, Tracing weathering regimes using the lithium isotope composition of detrital sediments. *Geology* **45**, 411–414 (2017).
- P. A. E. Pogge von Strandmann, M. T. Jones, A. J. West, M. J. Murphy, E. W. Stokke, G. Tarbuck, D. J. Wilson, C. R. Pearce, D. N. Schmidt, Lithium isotope evidence for enhanced weathering and erosion during the Paleocene-Eocene Thermal Maximum. *Advances* **7**, eabih4224 (2021).
- G.-Y. Wei, W. Wei, D. Wang, T. Li, X. Yang, G. A. Shields, F. Zhang, G. Li, T. Chen, T. Yang, H.-F. Ling, Enhanced chemical weathering triggered an expansion of euxinic seawater in the aftermath of the Sturtian glaciation. *Earth Planet. Sci. Lett.* **539**, 116244 (2020).
- Y. Sun, X. Li, Q. Liu, M. Zhang, P. Li, R. Zhang, X. Shi, In search of the inland Carnian Pluvial Event: Middle–Upper Triassic transition profile and U–Pb isotopic dating in the Yanchang Formation in Ordos Basin, China. *Geol. J.* **55**, 4905–4919 (2020).
- D. Wang, B. Xin, Y. Hua, F. Jinhua, Y. Jinli, Y. Zhang, Zircon SHRIMP U–Pb age and geological implications of tuff at the bottom of Chang-7 Member of Yanchang Formation in the Ordos Basin. *Sci. Chin. Earth Sci.* **57**, 2966–2977 (2014).
- J. Laskar, P. Robutel, F. Joutel, M. Gastineau, A. C. M. Correia, B. Levrard, A long-term numerical solution for the insolation quantities of the Earth. *A&A* **428**, 261–285 (2004).
- R. Zhang, Z. Jin, Q. Liu, P. Li, Z. Huang, J. Shi, Y. Ge, K. Du, Astronomical constraints on deposition of the Middle Triassic Chang 7 lacustrine shales in the Ordos Basin, Central China. *Palaeogeog., Palaeoclim., Palaeoecol.* **528**, 87–98 (2019).
- X. Li, Y. Zhang, Y. Sun, X. Shi, S. Zhang, Vegetation changes and climate shift during the latest Ladinian to the early Carnian: Palynological evidence from the Yanchang Formation, Ordos Basin, China. *Front. Earth Sci.* **10**, 1008707 (2023).
- X. Li, “Middle and Late Triassic Palynoflora and Paleoclimate in Ordos Basin,” thesis, Jilin University, Changchun, China (2023).
- J. Lu, P. Zhang, J. Dal Corso, M. Yang, P. B. Wignall, S. E. Greene, L. Shao, D. Lyu, J. Hilton, Volcanically driven lacustrine ecosystem changes during the Carnian Pluvial Episode (Late Triassic). *Proc. Natl. Acad. Sci.* **118**, e2109895118 (2021).
- P. Zhang, M. Yang, J. Lu, Z. Jiang, P. Vervoort, K. Zhou, X. Xu, H. Chen, Y. Wang, Z. He, X. Bian, L. Shao, J. Hilton, Four volcanically driven climatic perturbations led to enhanced continental weathering during the Late Triassic Carnian Pluvial Episode. *Earth Planet. Sci. Lett.* **626**, 118517 (2024).
- X. Yuan, S. Lin, Q. Liu, J. Yao, L. Wang, H. Guo, X. Deng, D. Cheng, Lacustrine fine-grained sedimentary features and organic-rich shale distribution pattern: A case study of Chang 7 Member of Triassic Yanchang Formation in Ordos Basin, NW China. *Petroleum Explor. Dev.* **42**, 37–47 (2015).
- A. d’Atri, F. Dela Pierre, R. Lanza, R. Ruffini, Distinguishing primary and resedimented vitric volcaniclastic layers in the Burdigalian carbonate shelf deposits in Monferrato (NW Italy). *Sediment. Geol.* **129**, 143–163 (1999).
- H. J. Haaland, H. Furnes, O. J. Martinsen, Paleogene tuffaceous intervals, Grane Field (Block 25/11), Norwegian North Sea: Their depositional, petrographical, geochemical character and regional implications. *Marine Petrol. Geol.* **17**, 101–118 (2000).
- J. Yoon, Lithium as a silicate weathering proxy: Problems and perspectives. *Aquatic Geochem.* **16**, 189–206 (2010).
- Q.-L. Wang, B. Chetelat, Z.-Q. Zhao, H. Ding, S.-L. Li, B.-L. Wang, J. Li, X.-L. Liu, Behavior of lithium isotopes in the Changjiang River system: Sources effects and response to weathering and erosion. *Geochim. Cosmochim. Acta* **151**, 117–132 (2015).
- T. R. Benson, M. A. Coble, J. H. Dilles, Hydrothermal enrichment of lithium in intracaldera illite-bearing claystones. *Advances* **9**, eadib8183 (2023).
- C. M. Fedo, H. Wayne Nesbitt, G. M. Young, Unraveling the effects of potassium metasomatism in sedimentary rocks and paleosols, with implications for paleoweathering conditions and provenance. *Geology* **23**, 921–924 (1995).
- J. Schüssler, R. Schoenberg, O. Sigmarsson, Iron and lithium isotope systematics of the Hekla volcano, Iceland — Evidence for Fe isotope fractionation during magma differentiation. *Chem. Geol.* **258**, 78–91 (2009).
- F. Álvarez-Amado, M. Rosales, L. Godfrey, C. Poblete-González, E. Morgado, M. Espinoza, A. Hidalgo-Gajardo, D. Volosky, J. Cortés-Aranda, The role of ignimbrites and fine sediments in the lithium distribution and isotopic fractionation in hyperarid environments: Insights from Li-isotopes in the Atacama Desert. *J. Geochem. Explor.* **241**, 107062 (2022).
- F. Cao, S. Yang, C. Yang, Y. Guo, L. Bi, Y. Li, Using lithium isotopes to quantitatively decode continental weathering signal: A case study in the Changjiang (Yangtze River) Estuary. *Sci. Chin. Earth Sci.* **64**, 1698–1708 (2021).
- W. Li, X.-M. Liu, O. A. Chadwick, Lithium isotope behavior in Hawaiian regoliths: Soil-atmosphere-biosphere exchanges. *Geochim. Cosmochim. Acta* **285**, 175–192 (2020).

47. R. Chen, G. Liu, F. Shang, Y. Cao, Nitrogen isotope compositions of the Upper Triassic Chang 7 Shale, Ordos Basin, North China: Implications for depositional redox conditions. *Marine Petrol. Geol.* **109**, 279–290 (2019).
48. Q. Liu, P. Li, Z. Jin, X. Liang, D. Zhu, X. Wu, Q. Meng, J. Liu, Q. Fu, J. Zhao, Preservation of organic matter in shale linked to bacterial sulfate reduction (BSR) and volcanic activity under marine and lacustrine depositional environments. *Marine Petrol. Geol.* **127**, 104950 (2021).
49. P. A. Meyers, R. Ishiwatari, Lacustrine organic geochemistry—An overview of indicators of organic matter sources and diagenesis in lake sediments. *Org. Geochem.* **20**, 867–900 (1993).
50. P. A. Meyers, E. Lallier-vergés, Lacustrine Sedimentary Organic Matter Records of Late Quaternary Paleoclimates. *J. Paleolimnol.* **21**, 345–372 (1999).
51. S. Meyers, Cracking the palaeoclimate code. *Nature* **546**, 219–220 (2017).
52. Q. Li, Y. Xu, C. Liang, L. Peng, Y. Zhou, Nitrogen removal by algal-bacterial consortium during mainstream wastewater treatment: Transformation mechanisms and potential N2O mitigation. *Water Res.* **235**, 119890 (2023).
53. Z. Zeng, H. Zhu, X. Yang, H. Zeng, X. Hu, C. Xia, The Pangaea Megamonsoon records: Evidence from the Triassic Mungaroo Formation, Northwest Shelf of Australia. *Gondwana Res.* **69**, 1–24 (2019).
54. X. Liu, Z. An, T. Rolph, X. Qiang, P. Hesse, H. Lu, J. Zhou, Y. Cai, Magnetic properties of the Tertiary red clay from Gansu. *Sci. Chin. Ser. D: Earth Sci.* **44**, 635–651 (2001).
55. H. Chang, Z. An, F. Wu, Z. Jin, W. Liu, Y. Song, A Rb/Sr record of the weathering response to environmental changes in westerly winds across the Tarim Basin in the late Miocene to the early Pleistocene. *Palaeogeog., Palaeoclim., Palaeoecol.* **386**, 364–373 (2013).
56. R. W. Murray, M. R. Buchholtz ten Brink, D. L. Jones, D. C. Gerlach, G. P. Russ III, Rare earth elements as indicators of different marine depositional environments in chert and shale. *Geology* **18**, 268–271 (1990).
57. H. W. Nesbitt, G. M. Young, Early Proterozoic climates and plate motions inferred from major element chemistry of lutites. *Nature* **299**, 715–717 (1982).
58. P. Wang, Y. Du, W. Yu, T. J. Algeo, Q. Zhou, Y. Xu, L. Qi, L. Yuan, W. Pan, The chemical index of alteration (CIA) as a proxy for climate change during glacial-interglacial transitions in Earth history. *Earth-Sci. Rev.* **201**, 103032 (2020).
59. S. M. McLennan, Weathering and Global Denudation. *J. Geol.* **101**, 295–303 (1993).
60. J. T. Parrish, F. Peterson, Wind directions predicted from global circulation models and wind directions determined from eolian sandstones of the western United States—A comparison. *Sedimen. Geol.* **56**, 261–282 (1988).
61. L. Zhang, C. Wang, P. B. Wignall, T. Kluge, X. Wan, Q. Wang, Y. Gao, Deccan volcanism caused coupled pCO<sub>2</sub> and terrestrial temperature rises, and pre-impact extinctions in northern China. *Geology* **46**, 271–274 (2018).
62. R. Millot, N. Vigier, J. Gaillardet, Behaviour of lithium and its isotopes during weathering in the Mackenzie Basin, Canada. *Geochim. et Cosmochim. Acta* **74**, 3897–3912 (2010).
63. R. Zhu, P. Zhao, L. Zhao, Tectonic evolution and geodynamics of the Neo-Tethys Ocean. *Sci. Chin. Earth Sci.* **65**, 1–24 (2022).
64. F. A. Macdonald, M. D. Schmitz, J. L. Crowley, C. F. Roots, D. S. Jones, A. C. Maloof, J. V. Strauss, P. A. Cohen, D. T. Johnston, D. P. Schrag, Calibrating the Cryogenian. *Science* **327**, 1241–1243 (2010).
65. R. Zhu, H. Wang, H. Wang, X. Wang, B. Wan, W. Zhang, H. Zhu, Y. Liu, J. Liu, Q. Meng, F. Hao, Z. Jin, Multi-spherical interactions and mechanisms of hydrocarbon enrichment in the Southeast Asian archipelagic tectonic system. *Sci. Chin. Earth Sci.* **67**, 566–583 (2024).
66. C. Zou, R. Zhu, Z.-Q. Chen, J. G. Ogg, S. Wu, D. Dong, Z. Qiu, Y. Wang, L. Wang, S. Lin, J. Cui, L. Su, Z. Yang, Organic-matter-rich shales of China. *Earth-Sci. Rev.* **189**, 51–78 (2019).
67. Z. Jin, R. Zhu, X. Liang, Y. Shen, Several issues worthy of attention in current lacustrine shale oil exploration and development. *Petrol. Explor. Dev.* **48**, 1471–1484 (2021).
68. D. Li, G. Luo, H. Yang, Z. She, D. Papineau, C. Li, Characteristics of the carbon cycle in late Mesoproterozoic: Evidence from carbon isotope composition of paired carbonate and organic matter of the Shennongjia Group in South China. *Precambrian Res.* **377**, 106726 (2022).
69. L. Zhang, T. J. Algeo, L. Zhao, Z.-Q. Chen, Z. Zhang, C. Li, Linkage of the late Cambrian microbe-metazoan transition (MMT) to shallow-marine oxygenation during the SPICE event. *Global Planet. Change* **213**, 103798 (2022).
70. B. Kalderon-Asael, J. A. R. Katchinoff, N. J. Planavsky, A. V. S. Hood, M. Dellinger, E. J. Bellefroid, D. S. Jones, A. Hofmann, F. O. Ossa, F. A. Macdonald, C. Wang, T. T. Isson, J. G. Murphy, J. A. Higgins, A. J. West, M. W. Wallace, D. Asael, P. A. E. P. von Strandmann, A lithium-isotope perspective on the evolution of carbon and silicon cycles. *Nature* **595**, 394–398 (2021).
71. Q. Li, S. Wu, D. Xia, X. You, H. Zhang, H. Lu, Major and trace element geochemistry of the lacustrine organic-rich shales from the Upper Triassic Chang 7 Member in the southwestern Ordos Basin, China: Implications for paleoenvironment and organic matter accumulation. *Marine and Petroleum Geology* **111**, 852–867 (2020).
72. S. Liu, S. Su, G. Zhang, Early Mesozoic basin development in North China: Indications of cratonic deformation. *J. Asian Earth Sci.* **62**, 221–236 (2013).
73. X. Jin, V. Baranyi, M. Caggiati, M. Franceschi, C. J. Wall, G. Liu, M. D. Schmitz, P. Gianolla, J. G. Ogg, G. Lu, Z. Shi, N. Preto, Middle Triassic lake deepening in the Ordos Basin of North China linked with global sea-level rise. *Global Planet. Change* **207**, 103670 (2021).
74. K. Zhang, R. Liu, Z. Liu, L. Li, Geochemical characteristics and geological significance of humid climate events in the Middle-Late Triassic (Ladinian-Carnian) of the Ordos Basin, central China. *Marine Petrol. Geol.* **131**, 105179 (2021).
75. Q.-R. Meng, G.-L. Wu, L.-G. Fan, H.-H. Wei, Tectonic evolution of early Mesozoic sedimentary basins in the North China block. *Earth-Sci. Rev.* **190**, 416–438 (2019).
76. R. Zhu, J. Cui, S. Deng, Z. Luo, Y. Lu, Z. Qiu, High-precision Dating and Geological Significance of Chang 7 Tuff Zircon of the Triassic Yanchang Formation, Ordos Basin in Central China. *Acta Geolog. Sinica* **93**, 1823–1834 (2019).

**Acknowledgments:** All the samples were collected from the Yanchang Oil Company. The Li contents and isotopes were measured at the Department of Earth and Planetary Sciences, Yale University, USA. We thank N. Planavsky of the Yale University for the constructive discussions.

**Funding:** This study was supported by the National Natural Science Foundation of China (grant nos. 42090020, U20B6001, 41625009, 42002139, and 42172151), the Strategic Priority Research Program of the Chinese Academy of Sciences, China (grant no. XDA14010404), and Tencent Xplorer Prize. **Author contributions:** Conceptualization: Q.L., P.L., L.J., Z.J., and D.Z. Methodology: Q.L., P.L., Z.J., and X.L. Validation: Q.L., L.J., Z.J., X.L., and R.Z. Formal analysis: Q.L., P.L., D.Z., Q.P., and R.Z. Investigation: Q.L., P.L., D.Z., Q.P., R.Z., and J.L. Resources: Q.L., P.L., Z.J., X.L., and Q.P. Data curation: Q.L., and Z.J. Writing—original draft: Q.L., P.L., and L.J. Writing—review and editing: Q.L., P.L., X.L., R.Z., and J.L. Visualization: Q.L., P.L., and J.L. Supervision: Q.L. Project administration: Q.L., and Z.J. Funding acquisition: Q.L., Z.J., and X. L. **Competing interests:** The authors declare that they have no competing interests. **Data and materials availability:** All data needed to evaluate the conclusions in the paper are present in the paper and/or the Supplementary Materials.

Submitted 11 May 2023

Accepted 14 February 2024

Published 15 March 2024

10.1126/sciadv.adl6594